Available online at www.sciencedirect.com
ScienceDirect
Journal of Power Sources 161 (2006) 264–274
JOURNAL OF POWER SOURCES
www.elsevier.com/locate/jpowsour

Characterisation of proton exchange membrane fuel cell (PEMFC) failures via electrochemical impedance spectroscopy

W. Mérida [a,*], D.A. Harrington [b], J.M. Le Canut [c], G. McLean [d]

[a] *Clean Energy Research Centre, University of British Columbia, Vancouver, BC, Canada V6T 1Z4*
[b] *Institute for Integrated Energy Systems, University of Victoria, Victoria, BC, Canada V8W 3P6*
[c] *Hydrogenics Corporation, 5985 McLaughlin Road, Mississauga, Ont., Canada L5R 1B8*
[d] *Angstrom Power Corporation, 106-980 West 1st Street, North Vancouver, BC, Canada V7P 3N4*

Received 18 February 2006; received in revised form 10 March 2006; accepted 28 March 2006
Available online 8 May 2006

Abstract

Two PEMFC failure modes (dehydration and flooding) were investigated using in situ electrochemical impedance spectroscopy (EIS) on a four-cell stack under load. The EIS measurements were made at different temperatures (70 and 80 °C), covering the current density range 0.1–1.0 A cm^{-2}, and the frequency range 0.1–2 × 10^5 Hz. Dehydration and flooding effects were observed in the frequency ranges 0.5–10^5 and 0.5–10^2 Hz, respectively.

We propose that impedance measurements at separate frequency ranges (or narrow bands thereof) can be used to distinguish between flooding and dehydration events. Similar approaches may be used to diagnose other important PEMFC failures.

Keywords: Fuel cell; Failure; Diagnosis; Impedance

1. Introduction

For fuel cells to reach consumer products, the relationship between their performance, lifetime, and failure mechanisms must be understood. The known failure patterns must be translated into industrial and commercial standards, quality control protocols, and safety or recycling regulations. The experimental methods available for failure diagnosis, degradation characterisation, and durability assessment have been reviewed by Wilkinson and St.-Pierre [1], Laconti et al. [2], and Fowler et al. [3,4]. The techniques discussed by these authors consider several PEMFC performance indicators including output voltage, membrane resistance, reactant permeability, water management, and they focus on specific designs or components.

Independent of the specific materials, topologies, or configurations fuel cells are characterised by their dependence on interfacial phenomena. The relevant physical processes (electron transfer, reactant diffusion, etc.) are controlled by the bulk properties of the different materials and, more importantly, by the interfacial characteristics between materials or phases. At each interface, the material properties change discontinuously and abruptly, and can become the limiting performance factors. Electrochemical impedance spectroscopy (EIS) is a technique especially well suited to characterise interfaces, and it can be used to characterise fuel cell performance non-invasively and in situ.

Although caution must be exercised in assigning physical processes to specific spectral features, EIS techniques provide powerful characterisation tools. Macdonald has published one of the best technical reviews available to date [5]. This review illustrates the progress made since Bauerle used EIS on zirconia–yttria compounds that can be used as the ionic conductors in solid-oxide fuel cells [6,7]. Since then, EIS measurements have also been made on phosphoric acid [8], molten carbonate [9], and direct methanol fuel cells [10,11]. More recently, EIS techniques in the context of PEMFC applications have resulted in a large number of publications [6–85]. A significant portion of these studies is devoted to materials development and component

* Correspondence to: Department of Mechanical Engineering, University of British Columbia, 6250 Applied Science Lane, Vancouver, BC, Canada V6T 1Z4. Tel.: +1 604 822 4189; fax: +1 604 82 2403.
E-mail address: wmerida@interchange.ubc.ca (W. Mérida).

0378-7753/$ – see front matter © 2006 Elsevier B.V. All rights reserved.
doi:10.1016/j.jpowsour.2006.03.067

Nomenclature

Δt_{dry}	total drying time (s)
ΔZ	impedance ratio between normal and simulated failure conditions
j	current density (A m^{-2})
j_0	amplitude of ac current density perturbation (A cm^{-2})
j_{dc}	dc current density (A cm^{-2})
λ_{O_2}	oxidant stoichiometry
λ_{H_2}	fuel stoichiometry
R_{stack}	stack resistance (Ω cm^2)
T	temperature (K)
θ_o	phase angle difference under normal conditions (°)
θ	phase angle difference between current and potential (°)
t_{dry}	time along a drying curve (s)
V_s	output from FRA's signal generator (V)
V_{dc}	dc bias from FRA's signal generator (V)
V_{ac}	ac perturbation from FRA's signal generator (V)
$\tilde{V}_k$	complex potential across cell k (k = 1–4) (V)
$\tilde{V}_T$	complex potential across stack (V)
$\tilde{V}_\Omega$	complex potential across shunt resistor (V)
V_{app}	attenuated input voltage to load bank (V)
V_{in}	input voltage to load bank (V)
Z	impedance (Ω cm^2)
Z'	real impedance component
Z''	imaginary impedance component
Z_W	Warburg impedance (Ω cm^2)
Z_o	impedance under normal conditions (Ω cm^2)

optimisation (for new catalysts, membranes, etc). For example, Springer and co-workers have developed models describing the electrical properties of different material layers in a PEMFC cathode. Their efforts have yielded one of the most complete descriptions of porous gas diffusion layers (GDLs) [80], and the prediction of expected features in the relevant impedance spectra. According to the flooded agglomerate model, the impedance spectra should present three arcs: one at high frequencies due to the double layer capacitance (charging through the charge transfer resistance); a mid-frequency arc (caused by the agglomerate dynamics); another arc at low frequencies (due to oxygen diffusion through the thin film). Experimental validation of these models and the potential uses of EIS as a characterisation technique have also been reported [41,81]. The measured spectra usually show only one or two arcs in the Nyquist plots covering the frequency range from 10^{-1} to 10^5 Hz [28]. These results have also been related to specific operating parameters in operating PEMFCs. Diard et al. have reported on EIS measurements made on a single cell with a small active area (25 cm^{-2}) operating at 80 °C under constant current load [17]. Their results show two depressed semi-circles, and large inductance effects at the high-frequency limit of the collected spectra (6.5 kHz). These effects and their causes are not discussed in detail.

The water content and ionic conductivity in Nafion and other membranes has also been the subject of EIS studies. Freire and Gonzalez have carried out studies on the impedance response of PEMFCs under varying humidification conditions [72]. The membrane materials, GDLs, and catalyst loadings were comparable to those used in the present work. The impedance measurement hardware, the imposed ac perturbation, and the reported frequency range (5 mHz to 20 kHz) were also similar to those considered here. Ciureanu and Roberge have described the potentiostatic measurements made on a single cell (active area = 25 cm^2) operating at 25 °C [14,15,71]. They also justify the adoption of a two-electrode measurement technique (with the anode functioning as both the auxiliary and reference electrodes). These approaches were evaluated independently and considered appropriate for the galvanostatic measurements reported in this work (see Section 2). In another publication, these authors discuss the potential use of EIS as a detection technique for catalyst poisoning (CO on Pt and Pt/Ru alloys) [14]. Large inductive effects were present in the low- and high-frequency limits of the collected spectra (10^{-2} and 10^4 Hz, respectively). The application of IES techniques for practical failure detection has also received attention recently.

In this work we propose that the measured spectral features can yield important information on potential failure modes, and more specifically, that EIS techniques can be used to distinguish between different failures in a PEMFC stack under load. Our experimental investigation focuses on water management failures, and considers two extremes: the dehydration in the membrane–electrode-assembly (MEA), and the presence of excess humidifying or product water.

Membrane dehydration reduces the protonic conductivity which can be approximated by changes in ohmic resistances. In contrast, the impedances associated with mass transport (e.g., diffusion within the electrode layers) require simulation via distributed circuit elements whose response varies with frequency [59–61,63–65]. Based on this analysis, we hypothesised that each failure corresponds to impedance changes that are observable at different frequency ranges. The hypothesis was tested experimentally by simulating the two failures in a small PEMFC stack and measuring the EIS spectra before, during, and after a simulated failure.

2. Experimental materials and methods

Our stack consisted of four cells connected in series, and separated by water-heated compartments. Individual cell and overall stack impedances were measured with the stack under load as illustrated in Fig. 1. Unlike conventional designs with a common manifold, each cell in the stack had separate inlet and outlet ports for the reactants. With reference to the numerals in Fig. 1, the cells consisted of two graphite bipolar plates (1), separated by a membrane electrode assembly (2), whose properties have been summarised in Table 1. Lateral manifolding plates (3) were fabricated to deliver the reactants to each cell individually. They were attached to alignment blocks perpendicular to the manifolding planes. Gold-plated copper plates (4) were used to collect the electronic current from the stack anode, deliver it

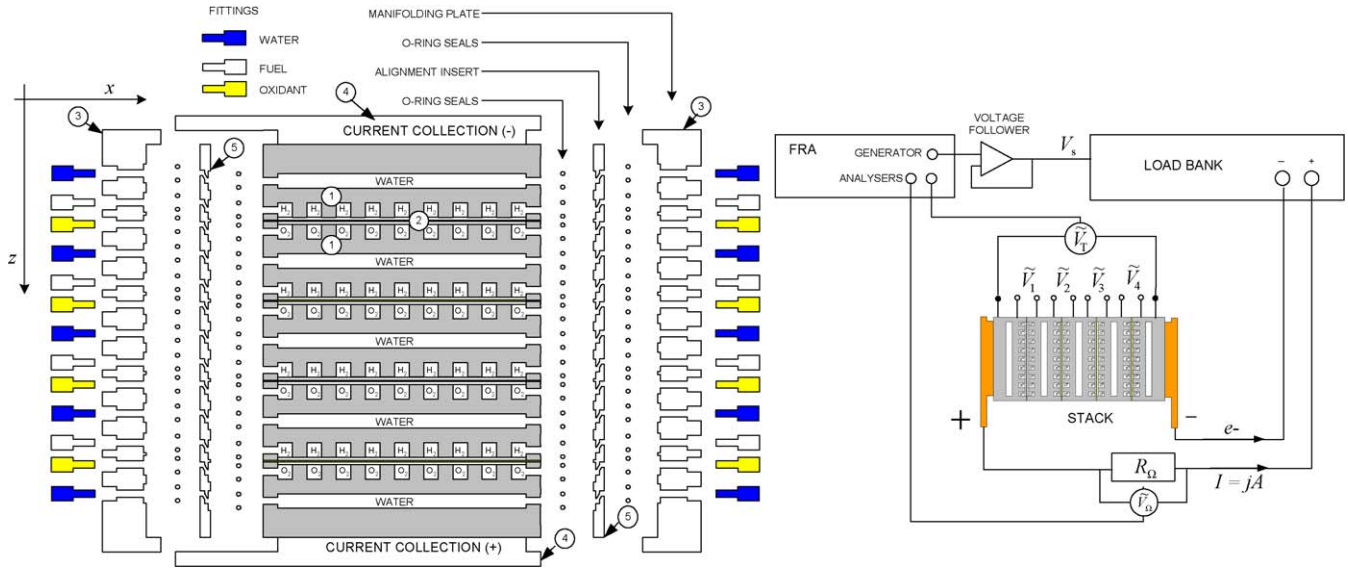

Fig. 1. The cross sectional view of the four-cell stack (left) and the functional modules required for impedance measurements (the illustration corresponds to the determination of Z_T).

to the load bank through a shunt resistor, and complete the circuit at the stack cathode. Four plastic inserts (5) were used to hold individual o-rings against each delivery port, and to accommodate small variations in MEA thickness. A pneumatic piston was used to control the stack sealing pressure along its longitudinal axis. This design made it possible to control the delivery and conditioning of reactants to individual cells, and to simulate single-cell failures without disturbing the steady state operation of the entire stack.

2.1. Membrane electrode assemblies (MEAs)

The MEA and single cell characteristics have been summarised in Table 1. The polymer area exceeded the active area (approximately 30 cm^2), and the extra polymer perimeter was used as the sealing surface for the inter-cell gaskets. Flooding and drying experiments were carried out using MEAs with ELAT/SS carbon cloth as the electrode substrate, and Nafion™ 115 as the ionic conductor. The manufacturing techniques for these MEAs are described elsewhere [86].

Table 1
Single cell properties and materials

	Value/description
MEA	
Gas diffusion layer (GDL) type	Carbon cloth
Ionic conductor	Nafion 115
Dry membrane thickness (m)	1.0×10^{-4}
Catalyst loading [anode] (cathode) (mg Pt cm^{-2})	[0.4] (2.0)
Active area (m^2)	3.08×10^{-3}
Uncompressed GDL thickness (m)	4.5×10^{-4}
Bipolar plates	
Material	Graphite
Plate thickness (m)	6.35×10^{-3}
Flow field pattern	Single serpentine
Channel cross-sectional area [fuel] (oxidant) (m^2)	[6.30×10^{-4}] (8.22×10^{-4})
Channel length [fuel] (oxidant) (m)	[2.44] (1.77)
Pressure drop at 2, 4, and 6 SLPM [fuel] (oxidant) (psi)	[1.5, 3.5, 5.5] (0.5, 1.0, 2.5)

2.2. Impedance measurements

A frequency response analyser (FRA) was connected to an electronic load as illustrated on the right of Fig. 1 (models 1255B from Solartron Analytical, and MCL488 from TDI-Dynaload, respectively). A voltage follower circuit was used to isolate grounds and unwanted current flow between the output signal from the FRA and the analog input to the load. The output signal, V_s, was the sum of a varying dc voltage (0–3 V dc), and an ac signal of small amplitude (5–20 mV rms):

$$V_s = V_{dc} + V_{ac} \sin(\omega t) \quad (1)$$

The steady state component, V_{dc}, controlled the dc current drawn from the stack (1 V = 10 A). The superimposed ac signal created a small, galvanostatic perturbation that generated voltage changes across a shunt resistor ($\tilde{V}_\Omega$), each individual cell ($\tilde{V}_k$, k = 1–4), and the overall stack ($\tilde{V}_T$). The frequency of this perturbation ranged from 0.5 Hz to approximately 200 kHz, and the high frequency limit was dictated by the cut-off frequency in the electronic load (20 kHz).

According to the load specifications, a frequency of 20 kHz in the control signal corresponds to an attenuation of −3 dB. However, we noted that the current perturbation amplitude was reduced, but not completely attenuated beyond this frequency. Even at higher attenuation rates (e.g., −12 dB/octave) the response amplitudes ($\tilde{V}_\Omega$, $\tilde{V}_{k,\,k=1-4}$, and $\tilde{V}_T$) were still within the sensitivity range of the FRA (see Fig. 2). Therefore,

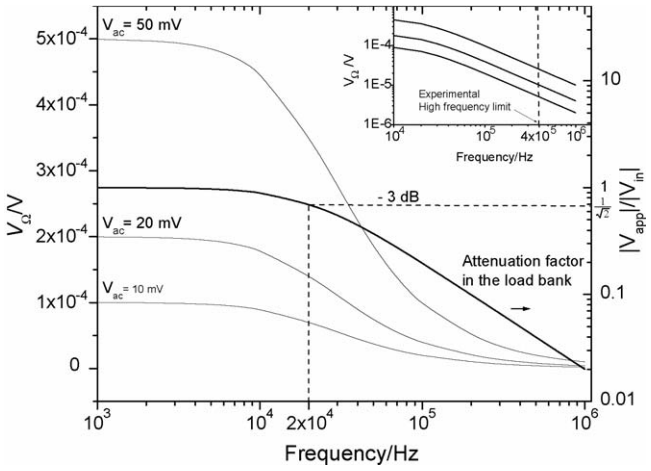

Fig. 2. The FRA sensitivity was sufficient to perform measurements beyond the load cut-off frequency (20 kHz) published by the manufacturer.

we were able to make meaningful and repeatable measurements beyond the high-frequency limit reported by the load manufacturer.

During a frequency sweep, the response across the shunt resistor, $\tilde{V}_\Omega$, and the response from one of these components were measured concurrently and the corresponding impedance was calculated directly:

$$\tilde{Z}_x = \frac{\tilde{V}_x R_\Omega}{\tilde{V}_\Omega}, \quad x \in \{1, \ldots, 4, T\} \tag{2}$$

Tildes indicate complex numbers that can be plotted as real and imaginary pairs on the Argand plane. In the discussion that follows, we use the notation Z' and Z'' for the real and imaginary parts of these pairs, respectively.

2.3. EIS limitations and experimental artefacts

Non-linearity and non-uniqueness represent two well-known limitations associated with EIS. In addition, the experimental setup on working PEMFCs must minimise or eliminate other sources of error.

For example, the potential thermal effects on R_Ω, must be addressed by minimising heat transfer via conduction. In our configuration, the maximum ohmic heating dissipated by the shunt was approximately 1 W (at 32 A dc delivered by the stack). This heating rate was insufficient to alter the shunt resistance significantly. The variation of R_Ω with frequency was also measured by connecting both analyser channels to the shunt resistor, and performing a frequency sweep. The measured value for R_Ω was $10^{-3}\,\Omega$ in the frequency range 0.1 to $\sim 10^4$ Hz. At higher frequencies, capacitive effects were detectable but very small. These effects are likely due to stray capacitances in the lead wires (i.e., they are unlikely to originate from the resistor).

The magnetic fields in the neighbourhood of the current leads connected to the stack can be significant even at moderate loads (e.g., 50 μT, 10 cm away from the centre of a cable carrying 5 A dc). As a result, inductive artefacts could be introduced by the position of the cables with relation to the stack. For example, placing the shunt resistor in the vicinity of a looping current cable resulted in large inductive loops in the impedance spectra at high frequencies (with correspondingly unphysical negative resistances). Other artefacts were generated by moving the cables or loosening the contacts between components (e.g., shunt to current cables, current cables to stack, etc). The importance of cell configuration in EIS measurements has received some attention [24], and the data reported in several publications includes signs of experimental artefacts. However, their causes and effects are seldom discussed in detail.

In this work, these effects were minimised by (i) fixing the cables and connections carefully, (ii) polishing and clamping all the metal contacts, (iii) twisting the large current leads to the electronic load, and (iv) maintaining equal lengths in the shielded, coaxial cables connected to the FRA. With these precautions, the impedance measurements were repeatable at each temperature and over the entire experimental frequency range ($0.5–2 \times 10^5$ Hz).

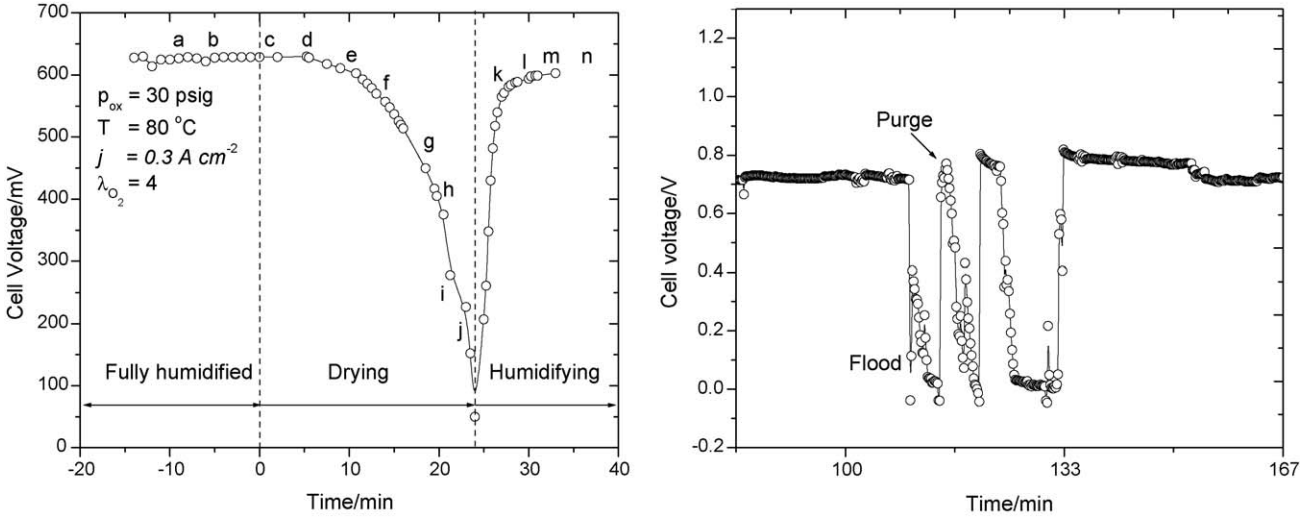

Fig. 3. The experimental curves for dehydration (left) and flooding (right). Points a, b, . . ., n on the dehydration curve correspond to the collected spectra.

3. Failure simulation

Dehydration was simulated by switching the oxidant in one cell between saturated and dry air streams at the same temperature (while maintaining constant humidification conditions in the remaining cells). The dehydrating cell and overall stack potentials were monitored while maintaining the other experimental parameters constant (temperature, pressure, gas flow, current density, etc.). EIS spectra were collected as the cell potential decreased and the varying spectra were compared to the spectrum collected prior to reactant switching (see Fig. 3). The drying process was allowed to continue until the cell potential dropped below 100 mV. At this point the oxidant streams were switched again and the cell re-humidified. At low current densities (e.g., $j = 0.1$, $0.2\,A\,cm^{-2}$) the reactant flows are smaller and the resulting drying curves progressed with increasingly negative slopes (i.e., different potential drop rates). This behaviour can be attributed to the water removal from of different layers within the MEA: at the beginning of a dehydration experiment, the excess water in the flow field channels and the surface of the GDL is removed first. As the drying process continues, water is removed from the porous GDL. In the final stages of dehydration, water is removed directly from the membrane and the dehydration process occurs more rapidly. At low current densities, irreversible membrane damage will occur in the final stages of a dehydration failure (thereby providing a few minutes for recovery measures). At higher current densities such as those required by automotive applications, the reactant flows are larger and the potentially irreversible damage occurs more rapidly. The time available to take corrective measures is thus reduced under these conditions.

Flooding failures were simulated by interfering with the oxidant flow downstream from an individual cell within the stack (thereby altering the reactant stoichiometry). Special attention was devoted to the cathode flows because the flooding effects are exacerbated by the presence of product water (in addition to the water carried by the saturated oxidant). EIS spectra were collected before and after flooding.

A flooding event consisted of a sudden drop in cell potential, followed by an intermittent potential profile (shown on the right side of Fig. 3). Unlike the features in the dehydration curves, the transitions between normal and flooded conditions were sudden. Data collection between states was difficult due to physical limitations in the flow controls. Consequently, and unlike the dehydration events, a flooding failure was very difficult to control. These limitations and potential improvements to the experimental techniques are being considered in the design of new hardware. The following paragraphs discuss the trends in the experimental results.

4. Results and discussion

Fig. 4 shows the typical polarisation curves obtained with the stack under steady state operation and with one cell under simulated failure (cell 2 under flooding). As expected, the sum of the measured impedances from each cell was equal to the overall stack impedance measured following the experimental setup in Fig. 1.

The experimental hardware made it possible to simulate failures in one cell without interrupting the steady state operation of the overall stack. A single cell failure had an effect on the performance of the stack and adjacent cells (e.g., by establishing small temperature gradients from cell to cell). However, the impedance measured across the cell under simulated failure was the largest contribution to the measured stack impedance. Although the cell impedances were measured individually, we report on the overall stack impedance (with one cell failing) because we consider that this is most practical implementation for a future detection technique or device (e.g., a two- or four-wire measurement across an entire stack instead of individual cell monitoring).

Fig. 5 shows the typical spectra collected on the stack with all the cells operating under normal conditions (at time = t_o) and with one cell operating under progressively more dehydrated conditions (at time = $t_{dry} > t_o$). This sequence also illustrates the graphical conventions used to report and summarise all the data hereinafter.

Unless otherwise indicated, the stack impedance was measured in the frequency range $0.5–2 \times 10^5$ Hz, using the components listed in Table 1, and under the experimental conditions listed in Table 2. The secondary plots superimposed on the upper

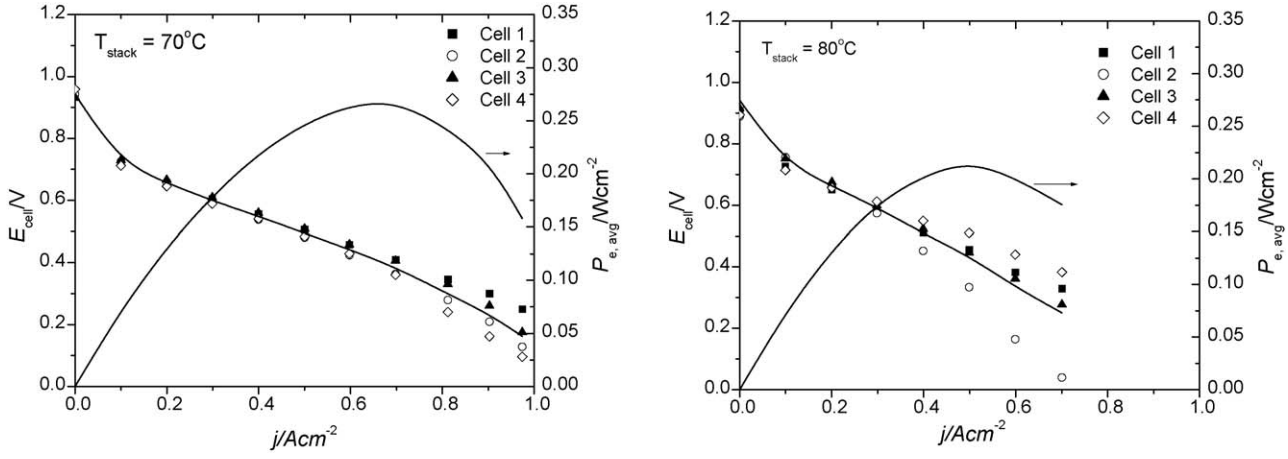

Fig. 4. The polarisation curves for the stack under steady state operating conditions (left) and with cell 2 under simulated flooding (right).

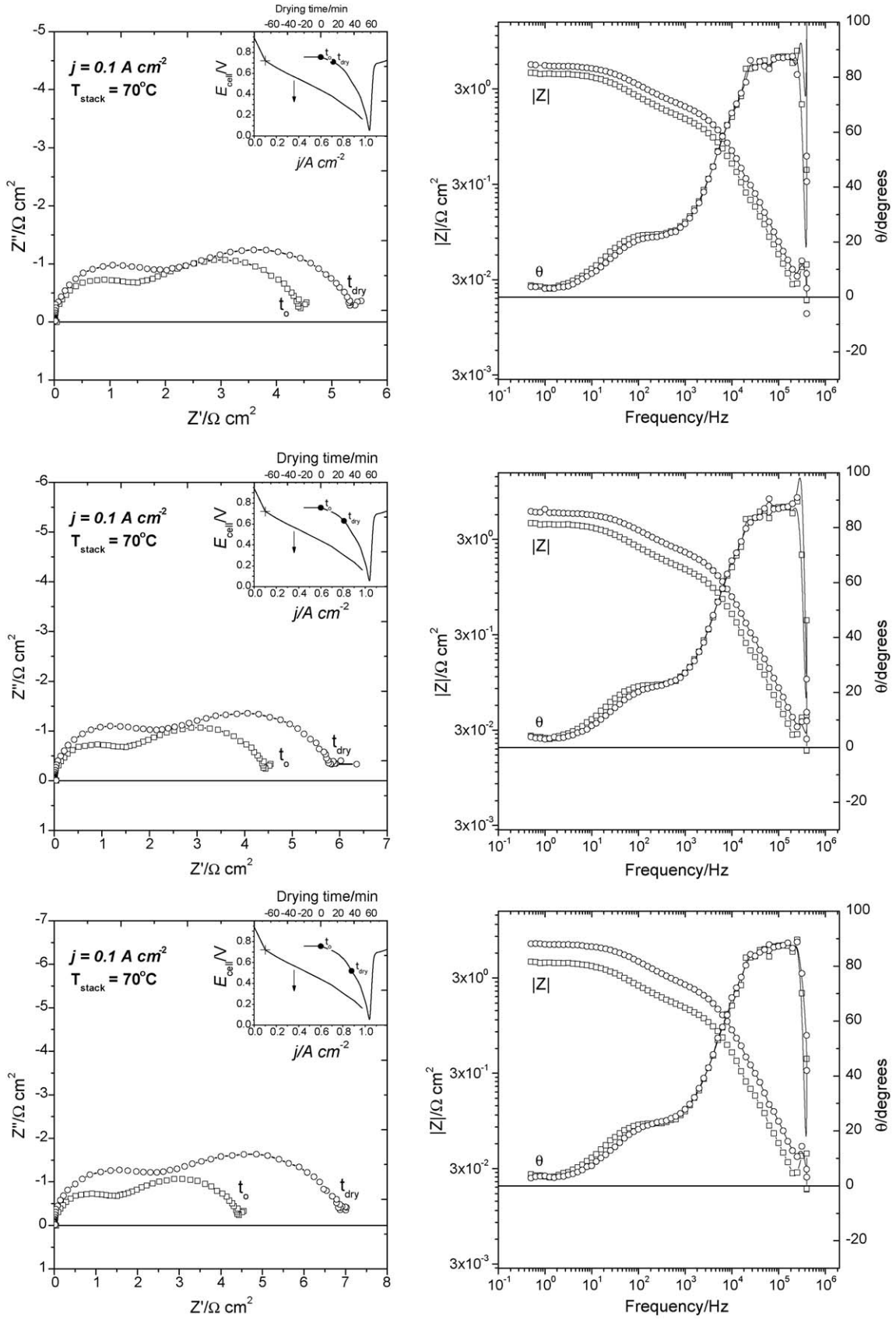

Fig. 5. Typical sequence of collected stack spectra under simulated dehydration in one cell.

Table 2
Experimental conditions

	Dehydration	Flooding
Fuel pressure (psig)	30	30
Oxidant pressure (psig)	30	30
Stack temperature (°C)	70	70
Humidification temperature [anode] (cathode) (°C)	[T_{stack} + 10] (T_{stack} + 10)	[T_{stack} + 10] (T_{stack} + 10)
Fuel stoichiometry	2	2
Oxidant stoichiometry	4	4–0
Longitudinal sealing pressure (psi)	120	120

right corner of the Argand planes provide two pieces of information: (i) they indicate the cell's operating point at the beginning of a simulated failure event (i.e., the point on the polarisation curve plotted on their bottom and left axis) and (ii) they show the points along the dehydration or flooding curves that varied as each experiment progressed.

Similar measurements were made at higher current densities and different temperatures. For brevity, the measurements under dehydration at illustrative current densities have been summarised by Fig. 6. Furthermore, the Bode plots are not included explicitly in this figure or in the remaining impedance spectra reported here. In all cases, the complex data on the Nyquist plots are equivalent.

As illustrated in Fig. 6, the dehydration experiments revealed an overall and monotonic increase in the stack's impedance as the failing cell became progressively more dehydrated (i.e., from point a to point f along the dehydration curve inset in Fig. 6). The salient feature during the dehydration experiments was the increase in the stack impedance across the entire experimental frequency range (including the high frequency range above a few kHz). These results are consistent with impedance changes dominated by an increase in the ohmic resistance at the membrane.

Larger current loads required larger reactant flows with larger drying rates, and correspondingly shorter drying times. Consequently, the number of spectra collected between drying events was progressively smaller as the current load increased. The spectra collected do not correspond to a single point on the drying curves, but rather to an interval defined by the time required to collect the spectrum. Depending on the number of frequencies per decade and the low frequency limits, the collection times ranged from tens of seconds to a few minutes.

The recovery time upon re-humidification was too short to collect multiple spectra between fully dehydrated and fully re-humidified conditions (e.g., between points f and g in Fig. 6). To prevent ohmic overheating and potential irreversible damage to the membrane, the drying cell was always prevented from reaching potentials below 20 mV dc. This required rapid switching from dry to humidified oxidant streams.

The results under typical flooding simulations are summarised in Fig. 7. The simulated failures produced no variations in the high-frequency arcs of the measured impedance spectra. These results are consistent with constant membrane humidification between normal and flooded conditions (i.e., the membrane resistance corresponds to fully humidified conditions in both cases).

The measured flooding effects on impedance were small but detectable (e.g., the change in magnitude is smaller than 1 Ω cm^2 at j = 0.1, 0.3, and 0.5 A cm^{-2}). Unlike the dehydration effects, the flooding variations were not present over the entire

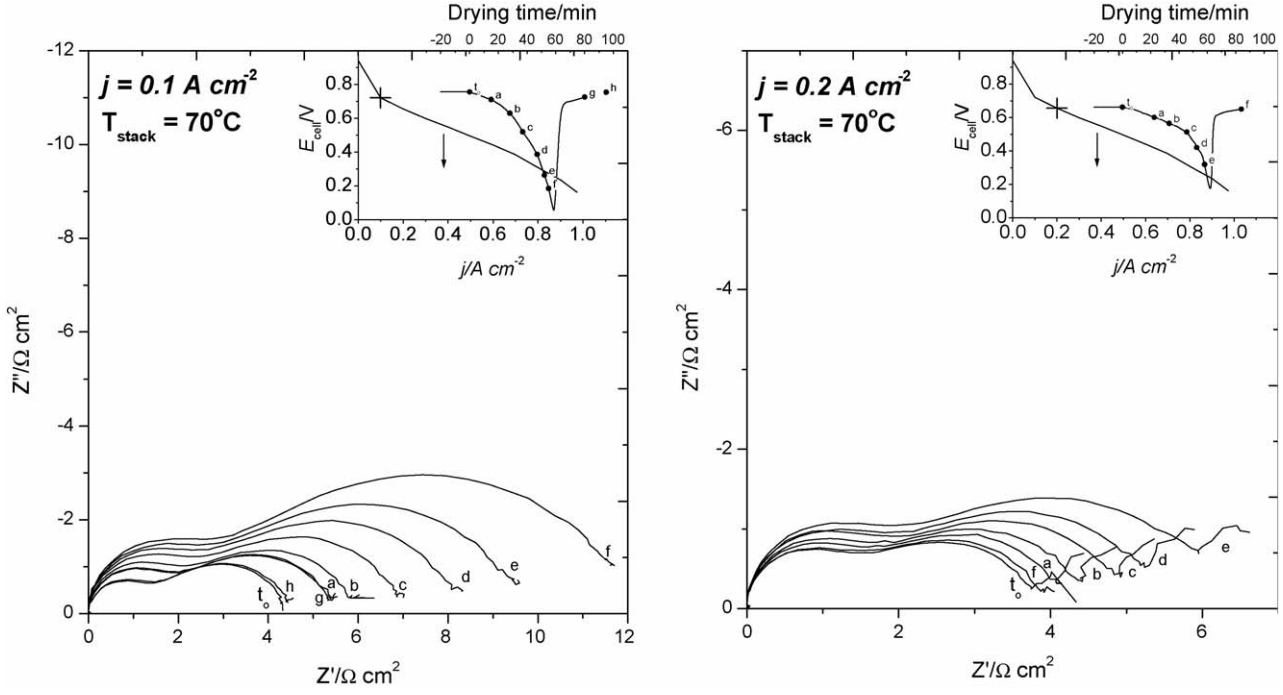

Fig. 6. Measured stack impedance with one cell under dehydration at 70 °C. j = 0.1 A cm^{-2} (left) and j = 0.2 A cm^{-2} (right).

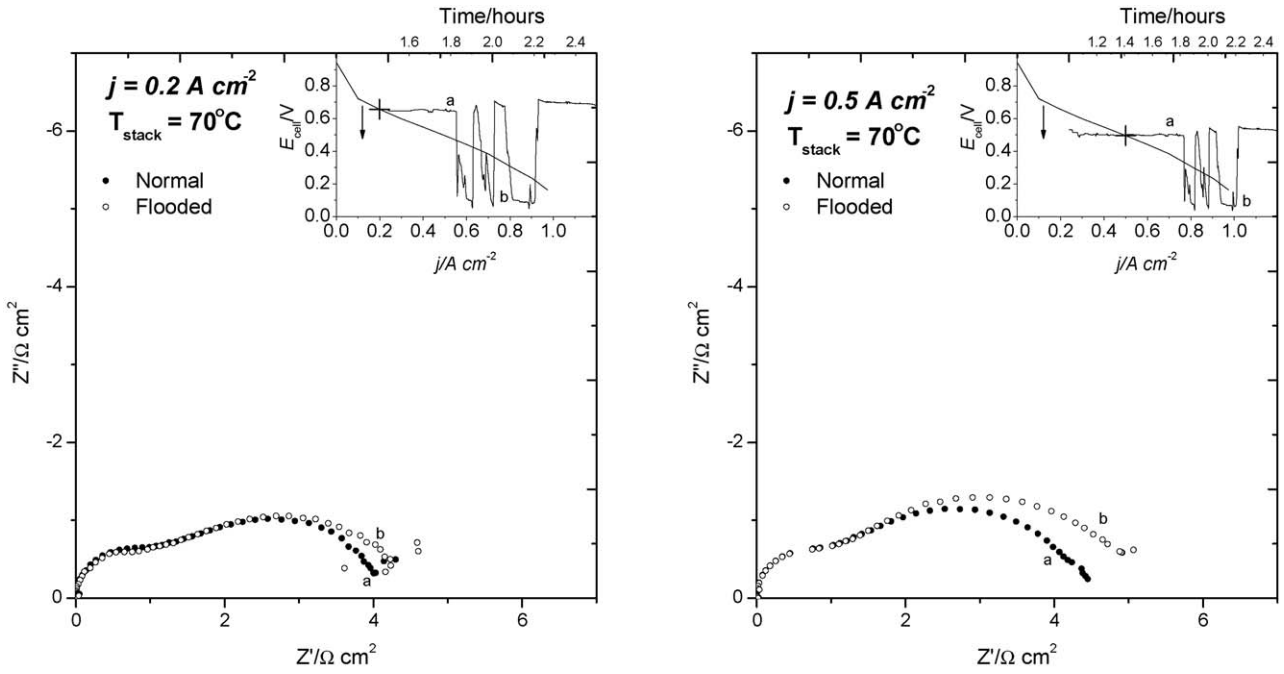

Fig. 7. Measured stack impedance with one cell onder simulated flooding at 70 °C. $j = 0.2\ \mathrm{A\,cm^{-2}}$ (left) and $j = 0.5\ \mathrm{A\,cm^{-2}}$ (right).

experimental frequency range, and they were only detected between 0.5 and 10^2 Hz. Although it is the focus of current efforts, our objective in this work was not to provide a detailed investigation of the underlying physical phenomena causing the changes in impedance. We propose that by monitoring these changes over different frequency ranges (or narrow bands thereof), it may be possible to detect and distinguish two or more failure modes.

Practical and inexpensive detection systems are unlikely to measure real and imaginary impedance components separately, or to cover wide frequency ranges. Measuring the variation of impedance amplitude- or phase-angle ratios over narrow frequency bands may be simpler and more economical. Fig. 8 has been used to summarise the change in the impedance magnitude with frequency. This change was quantified by the ratio $\Delta Z = |Z|/|Z_o|$, where Z corresponds to the overall stack

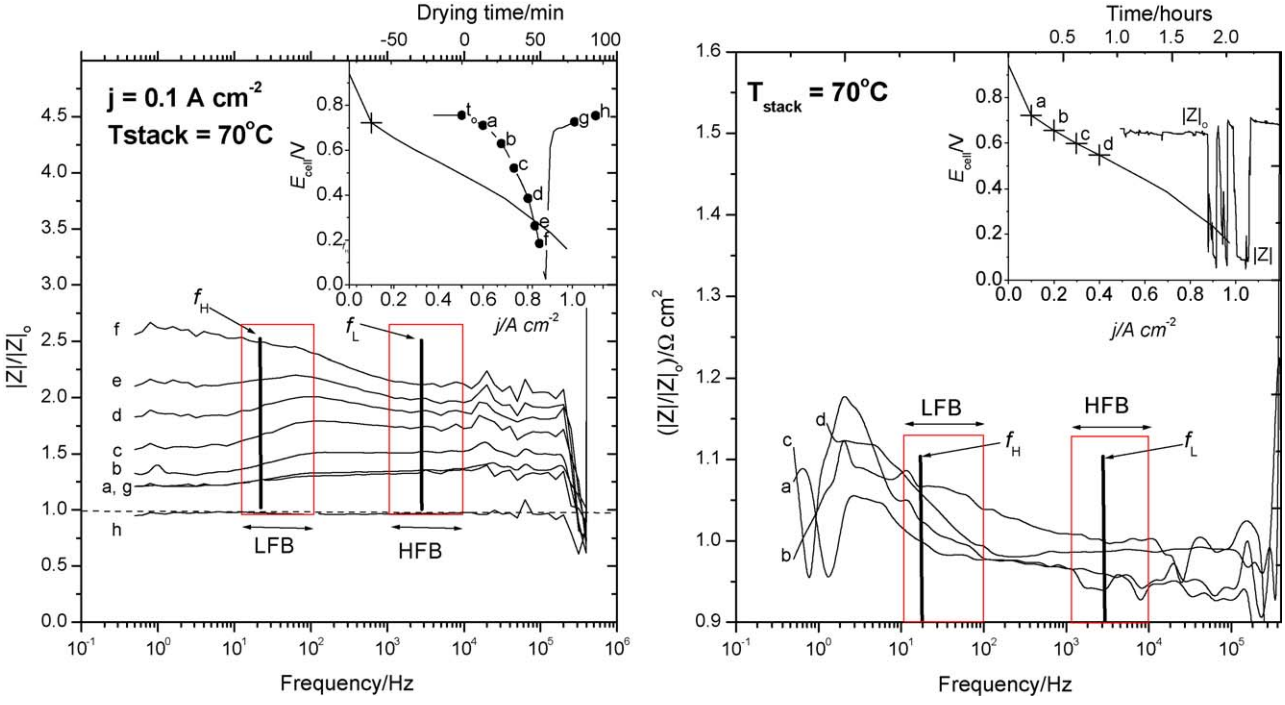

Fig. 8. Measured change in impedance magnitude ratios for dehydrating (left) and flooding conditions (right). Concurrent impedance measurements at high- and low-frequency bands (HFB and LFB) can be used to distinguish between two failure modes.

impedance measured along the drying curves (with once cell failing), and Z_o corresponds to the stack impedance measured under normal operating conditions (i.e., the impedance magnitude prior to the simulated failure in one cell).

As illustrated, the amplitude ratios under dehydrating conditions are large and relatively constant over a wide frequency range, and as expected, the magnitude ratio calculated from the measurements before dehydration and after recovery was very close to unity. In Fig. 8 two arbitrary frequency bands have been indicated. A single frequency in each band (f_L and f_H) could suffice to diagnose the failure: large impedance variations (>5%) at high frequencies ($f > 103$ Hz) can be associated with dehydration. Smaller variations (<10%) at low frequencies without concurrent changes at high frequencies can be associated with flooding.

The net water transport rates within the MEA are the result of complex and highly coupled mechanisms. Further experiments are required to elucidate these mechanisms, and the individual phenomenological contributions to the impedance spectrum. The design of such experiments is the focus of ongoing efforts at our laboratories. With measurements at carefully chosen frequency combinations, Harrington and Mérida have proposed that these techniques may be sufficient for the specifications of practical detection hardware and techniques [87].

5. Conclusions

EIS measurements have been used to characterize the macroscopic effects of dehydration and flooding on the impedance of PEMFCs. The two failure modes were simulated on individual cells within a four-cell stack under load. The dehydration effects were measurable over the frequency range 0.5–100 kHz, while the flooding effects were measurable in the frequency range 0.5–100 Hz.

These results illustrate that separate or concurrent impedance measurements in distinct frequency ranges (or narrow bands thereof) may be used to identify the two failure modes semi-instantaneously (the detection time being limited by the response or acquisition time in an eventual diagnosis device).

Acknowledgements

The authors would like to acknowledge the Advanced Systems Institute of British Columbia and Hydrogenics Test Systems (formerly Greenlight Power Technologies) for their funding of this work and the projects associated with it.

References

[1] D.P. Wilkinson, J. St.-Pierre, Durability, in: W. Vielstich, A. Lamm, H.A. Gasteiger (Eds.), Handbook of Fuel Cells, John Wiley & Sons, Etobicoke, Ontario, 2003, pp. 611–626 (Chapter 47).
[2] A.B. Laconti, M. Hamdan, R.C. McDonald, Mechanisms of membrane degradation, in: W. Vielstich, A. Lamm, H.A. Gasteiger (Eds.), Handbook of Fuel Cells, John Wiley & Sons, Etobicoke, Ontario, 2003, pp. 647–662 (Chapter 49).
[3] M.W. Fowler, J.C. Amphlett, R.F. Mann, B.A. Peppley, P.R. Roberge, Issues associated with voltage degradation in a polymer electrolyte fuel cell stacks, J. New Mater. Electrochem. Syst. 5 (2002) 255–262.
[4] M.W. Fowler, J.C. Amphlett, R.F. Mann, B.A. Peppley, P.R. Roberge, Incorporation of voltage degradation into a generalized steady state electrochemical model for a PEM fuel cell, J. Power Sources 106 (2002) 274–283.
[5] J.R. Macdonald, in: E. Barsoukov (Ed.), Impedance Spectroscopy Theory, Experiment, Applications, second ed., John Wiley & Sons, Toronto, 2005.
[6] J.E. Bauerle, Study of solid electrolyte polarisation by a complex admittance method, J. Phys. Chem. Solids 30 (1969) 2657–2670.
[7] N. Wagner, W. Schnurnberger, B. Müller, M. Lang, Electrochemical impedance spectra of solid-oxide fuel cells and polymer membrane fuel cells, Electrochim. Acta 43 (24) (1998) 3785–3793.
[8] J.M. Song, S.Y. Cha, W.M. Lee, Optimal composition of polymer electrolyte fuel cell electrodes determined by the AC impedance method, J. Power Sources 94 (1) (2001) 78–84.
[9] P. Tomczyk, M. Mosialek, Investigation of the oxygen electrode reaction in basic molten carbonates using electrochemical impedance spectroscopy, Electrochim. Acta 46 (2001) 3023–3032.
[10] Jens T. Müller, Peter M. Urban, Characterization of direct methanol fuel cells by ac impedance spectroscopy, J. Power Sources 75 (1998) 139–143.
[11] Jens T. Müller, Peter M. Urban, Wolfgang F. Hölderich, Impedance studies on direct methanol fuel cell anodes, J. Power Sources 84 (1999) 157–160.
[12] A.S. Aricò, V. Antonucci, V. Alderucci, E. Modica, N. Giordano, A.C.-impedance spectroscopy study of oxygen reduction at nafion coated gas-diffusion Electrodes in sulphuric acid: teflon loading and methanol cross-over effects, J. Appl. Electrochem. 23 (1993) 1107–1116.
[13] C. Boyer, S. Gamburzev, O. Velev, S. Srinivasan, A.J. Appleby, Measurements of proton conductivity in the active layer of PEM fuel cell gas diffusion electrodes, Electrochim. Acta 43 (24) (1998) 3703–3709.
[14] M. Ciureanu, H. Wang, Z. Qi, Electrochemical impedance study of membrane–electrode assemblies in PEM fuel cells: II. Electrooxidation of H_2 and H_2/Co mixtures on Pt/Ru-based gas diffusion electrodes, J. Phys. Chem. B (103) (1999) 9645–9657.
[15] M. Ciureanu, H. Wang, Electrochemical impedance study of anode CO-poisoning in PEM fuel cells, J. New Mater. Electrochem. Syst. 3 (2000) 107–119.
[16] K. Darowicki, Differential analysis of impedance data, Electrochim. Acta 43 (16–17) (1998) 2281–2285.
[17] J.P. Diard, B. Le Gorrec, C. Montella, G. Poinsignon, G. Vitter, Impedance measurements of polymer electrolyte membrane fuel cells running on constant load, J. Power Sources 74 (1998) 244–245.
[18] J.P. Diard, B. Le Gorrec, C. Montella, Linear diffusion impedance. general expression and applications, J. Electroanal. Chem. 471 (1999) 126–131.
[19] C.A. Edmondson, P.E. Stallworth, M.C. Wintersgill, J.J. Fontanella, Y. Dai, S.G. Greenbaum, Electrical conductivity and NMR studies of methanol/water mixtures in Nafion membranes, Electrochim. Acta 43 (10–11) (1998) 1295–1299.
[20] J. Geyer, H. Kohlmüller, H. Landes, R. Stübner, Investigations into the kinetics of the Ni-YSZ-Cermet-Anode of a solid oxide fuel cell, in: Proceedings of Fifth International Symposium on SOFC, 1997.
[21] J.P. Diard, B. Le Gorrec, C. Montella, C. Poinsignon, G. Vitter, Impedance measurements of polymer electrolyte membrane fuel cells running on constant load, J. Power Sources 74 (1998) 244–245.
[22] H. Holdik, A. Alcaraz, P. Ramírez, S. Mafé, Electric field enhanced water dissociation at the bipolar membrane junction from ac impedance spectra measurements, J. Electroanal. Chem. 442 (1998) 13–18.
[23] F. Josse, R. Lukas, R. Zhou, S. Schneider, D. Everhart, AC-impedance-based chemical sensors for organic solvent vapors, Sens. Actuators B 35–36 (1996) 363–369.
[24] T. Kato, A. Momma, Y. Kaga, S. Nagata, Y. Kasuga, M. Kitase, Influence of cell configuration on measuring interfacial impedances between a solid electrolyte and an electrode, Solid State Ionics 132 (2000) 287–295.
[25] J. Macdonald, Ross, Impedance Spectroscopy Emphasizing Solid Materials and Systems, John Wiley & Sons, Toronto, 1987.
[26] S. Primdahl, M. Mogensen, Gas conversion impedance: SOFC anodes in H_2/H_2O atmospheres, in: Proceedings of Fifth International Symposium on SOFC, 1997.

[27] S.A.M. Refaey, G. Schwitzgebel, O. Schneidner, Electrochemical impedance studies on oxidative, overoxidative degradation, deactivation and reactivation of conducting polymers, Synth. Met. 98 (1998) 183–192.
[28] K. Roßberg, L. Dunsch, Electrochemical impedance spectroscopy on conducting polymer membranes, Electrochim. Acta 44 (1999) 2061–2071.
[29] S. Kjelstrup, P. Pugazhendi, D. Bedeaux, Impedance of the hydrogen polymer fuel cell electrode. Theory and experiments, Zeitschrift für Physikalische Chemie 214 (7) (2000) 895–916.
[30] S.J. Schiefelbein, D.R. Sadoway, A high-accuracy, calibration-free technique for measuring the electrical conductivity of molten oxides, Metall. Mater. Trans. B 28B (1997) 1141–1149.
[31] S.J. Schiefelbein, N. Fried, K.G. Rhoads, D.R. Sadoway, A high-accuracy, calibration-free technique for measuring the electrical conductivity of liquids, Rev. Sci. Instrum. 69 (9) (1998) 3308–3313.
[32] T. Van Nguyen, N. Vanderborgh, The rate of isothermal hydration of polyperfluorosulfonic acid membranes, J. Membr. Sci. 143 (1998) 235–248.
[33] M.C.W. Fontanella, J. John, Complex impedance measurements on Nafion, Electrochim. Acta 43 (10–11) (1998) 1533–1538.
[34] S.-I. Pyun, Y.-G. Ryu, A study of oxygen reduction on platinum-dispersed porous carbon electrodes at room and elevated temperatures by using ac impedance spectroscopy, J. Power Sources 62 (1996) 1–7.
[35] M. Lang, R. Henne, G. Schiller, N. Wagner, Production and characterization of vacuum plasma sprayed anodes for solid oxide fuel cells, in: Proceedings of Fifth International Symposium on SOFC, 1997.
[36] K.M. Nouel, P.S. Fedkiw, Nafion-based composite polymer electrolyte membranes, Electrochim. Acta 43 (16–17) (1998) 2381–2387.
[37] T. Okada, S. Møller-Host, O. Gorseth, S. Kjelstrup, Transport and equilibrium properties of Nafion membranes with H^+ and Na^+ ions, J. Electroanal. Chem. 442 (1998) 137–145.
[38] A. Parthasathy, B. Davé, S. Srinivasan, A.J. Appleby, The platinum microelectrode/Nafion interface: an electrochemical impedance spectroscopic analysis of oxygen reduction kinetics and Nafion characteristics, J. Electrochem. Soc. 139 (6) (1992) 1634–1641.
[39] C.C. Boyer, R.G. Anthony, A.J. Appleby, Design equations for optimized PEM fuel cell electrodes, J. Appl. Electrochem. 30 (2000) 777–786.
[40] S.J.C. Cleghorn, C.R. Derouin, M.S. Wilson, S. Gottesfeld, A printed circuit approach to measuring current distribution in a fuel cell, J. Appl. Electrochem. 28 (1998) 663–672.
[41] T.E. Springer, T.A. Zawodzinski, M.S. Wilson, S. Gottesfeld, Characterization of polymer electrolyte fuel cells using ac impedance spectroscopy, J. Electrochem. Soc. 143 (2) (1996) 587–599.
[42] M. Ciureanu, H. Wang, Electrochemical impedance study of membrane–electrode assemblies in pem fuel cells: I. electrooxidation of H_2 and H_2/Co mixtures on Pt/Ru-based gas diffusion electrodes, J. Electrochem. Soc. 146 (11) (1999) 4031–4040.
[43] A. Eisenberg, Macromolecules 3 (1970) 147.
[44] T.D. Gierke, J. Electrochem. Soc. (1977) (Proceedings Abstract).
[45] S.W. Yeo, A. Eisenberg, J. Appl. Polym. Sci. 21 (1977) 875.
[46] E.J. Roche, M. Pineri, R. Duplessix, A.M. Levelut, J. Polym. Sci. Polym. Phys. Ed. 2 (1982) 107.
[47] T.D. Gierke, G.E. Munn, F.C. Wilson, J. Polym. Sci. Polym. Phys. Ed. 19 (1981) 1687.
[48] M. Fujimara, T. Hashimoto, H. Kawai, Macromolecules 14 (1981) 139.
[49] C. Gavach, G. Pamboutzouglou, M. Nedyalkov, G. Pourcelly, J. Membr. Sci. 45 (1989) 37.
[50] P. Debye, Polar Molecules, Chemical Catalogue Company, New York, 1929.
[51] J. Llopis, F. Colom, Study of the impedance of a platinum electrode acting as anode, in: Proceedings of The Eighth Meeting of the CITCE, Madrid, 1958.
[52] W. Weperen, B.P. van, M. Lenting, E.J. Bijrank, H.W. der Hartog, Effect of the Ce^{3+} concentration on the reorientation of dipoles in SrF_2:Ce^{3+}, Phys. Rev. B 16 (1977) 1953–1958.
[53] K.S. Cole, R.H. Cole, Dispersion and absorption in dielectrics I. Alternation current characteristics, J. Chem. Phys. 9 (1941) 341–351.
[54] T.D. Gierke, T.D. Hsu, Perfluorinated Ionomer Membranes, American Chemical Society, Washington, DC, 1982.
[55] S.W. Yeo, J. Electrochem. Soc. 130 (1983) 533.
[56] G. Pourcelly, A. Oikonomou, C. Gavach, H.D. Hurwitz, Influence of the water content on the kinetics of counter-ion transport in perfluorosulphonic membranes, J. Electroanal. Chem. 287 (1) (1990) 43–59.
[57] T.A. Zawodzinski, M. Neeman, L.O. Sillerud, S. Gottesfeld, J. Phys. Chem. 95 (1991) 6040.
[58] T.A. Zawodzinski Jr., et al., A comparative study of water uptake by and transport through ionomeric fuel cell membranes, J. Electrochem. Soc. 140 (1993) 1981.
[59] D.R. Franceschetti, J.R. McDonanld, Diffusion of neutral and charged species small-signal A.C. conditions, J. Electroanal. Chem. 101 (1979) 307–316.
[60] J.R. Macdonald, Theory of a.c. space–charge polarization effects in photoconductors, semiconductors and electrolytes, Phys. Rev. 92 (1953) 4–17.
[61] J.R. Macdonald, Electrical response of materials containing space charge with discharge at the electrodes, J. Chem. Phys. 54 (1971) 2026–2050.
[62] J.R. Macdonald, The impedance of a galvanic cell with two plane-parallel electrodes at a short distance, J. Electroanal. Chem. 32 (1971) 317–328.
[63] J.R. Macdonald, Binary electrolyte small-signal frequency response, J. Electroanal. Chem. 53 (1974) 1–55.
[64] J.R. Macdonald, Simplified impedance/frequency-response for intrinsically conducting solids and liquids, J. Chem. Phys. 61 (1974) 3977–3996.
[65] J.R. Macdonald, D.R. Franceschetti, Theory of small signal ac response of solids and liquids with recombining mobile charge, J. Chem. Phys. 68 (1978) 1614–1637.
[66] J.W. Wei, C. Stone, A.E. Steck, US Patent 5,422,411 (1995).
[67] A.K. Jonscher, Physical basis of dielectric loss, Nature 253 (1975) 717–719.
[68] J.R. Macdonald, Note on the parameterization of the constant-phase admittance element, Solid State Ionics 13 (1984) 147–149.
[69] F.N. Büchi, S. Srinivasan, Operating proton exchange membrane fuel cells without external humidification of the reactant gases, J. Electrochem. Soc. 144 (8) (1997) 2767–2772.
[70] Mulder, et al., J. Electroanal. Chem. 285 (1990) 103–115.
[71] M. Ciureanu, R. Roberge, Electrochemical impedance study of PEM fuel cells. Experimental diagnostics and modeling of air cathodes, J. Phys. Chem. B 105 (17) (2001) 3531–3539.
[72] T.J.P. Freire, E.R. Gonzalez, Effect of membrane characteristics and humidification conditions on the impedance response of polymer electrolyte fuel cells, J. Electroanal. Chem. 503 (1–2) (2001) 57–68.
[73] R.C. Hughes, W.G. Yelton, K.B. Pfeifer, S.V. Patel, Characteristics and mechanisms in ion-conducting polymer films as chemical sensors, J. Electrochem. Soc. 148 (4) (2001) H37–H44.
[74] J.D. Kim, Y.I. Park, K. Kobayashi, M. Nagai, M. Kunimatsu, Characterization of CO tolerance of PEMFC by ac impedance spectroscopy, Solid State Ionics 140 (3–4) (2001) 313–325.
[75] J.T. Müller, P.M. Urban, Characterization of direct methanol fuel cells by AC impedance spectroscopy, J. Power Sources 75 (1) (1998) 139–143.
[76] J.T. Müller, P.M. Urban, W.F. Hölderich, Impedance studies on direct methanol fuel cell anodes, J. Power Sources 84 (1999) 157–160.
[77] V.A. Paganin, C.L.F. Oliveira, E.A. Ticianelli, T.E. Springer, E.R. Gonzalez, Modelistic interpretation of the impedance response of a polymer electrolyte fuel cell, Electrochim. Acta 43 (24) (1998) 3761–3766.
[78] C. Poinsignon, B. Le Gorrec, G. Vitter, C. Montella, J.P. Diard, Control of a running H2/O2 fuel cell with filled polymeric membranes by impedance spectroscopy, in: Proceedings of Materials Research Society Symposium, Proceedings, v575, 2000, Proceedings of the 1999 MRS Spring Meeting, Symposium CC New Materials for Batteries and Fuel Cells, San Francisco, CA, USA, 2000.
[79] R.H. Song, D.J. Kim, C.S. Kim, D.R. Shin, Electrochemical evaluation of single cell in phosphoric acid fuel cell by ac impedance technique, J. New Mater. Electrochem. Syst. 4 (1) (2001) 47–50.
[80] T.E. Springer, I.D. Raistrick, Electrical impedance of a pore wall for the flooded-agglomerate model of porous gas-diffusion electrodes, J. Electrochem. Soc. 136 (6) (1989) 1594–1603.
[81] T.E. Springer, M.S. Wilson, S. Gottesfeld, Modeling and experimental diagnostics in polymer electrolyte fuel cells, J. Electrochem. Soc. 140 (12) (1993) 3513–3526.

[82] P. Beattie, et al., Ionic conductivity of proton exchange membranes, J. Electroanal. Chem. 503 (2001) 45–56.
[83] S.L.A. da Silva, E. Ticianelli, 1995.
[84] G. Spinolo, G. Chiodello, A. Magistris, U. Anselmi-Tamburini, Dataweighting, J. Electrochem. Soc. 135 (1998) 1419.
[85] J.P. Diard, B. Le-Gorrec, C. Montella, Cinétique électrochimique. Hermann Éditeurs des Sciences et des Arts 293 rue Lecourbe 75015, Paris, 1996.
[86] M.S. Wilson, Membrane catalyst layer for fuel cells. US Patent 5,234,777 Application August 10, 1993, Assignee: The Regents of the University of California, 1993.
[87] D.A. Harrington, W. Mérida, Methods and apparatus for indicating a fault condition in fuel cells and fuel cell components. US Patent Application 20,040,091,759, Assignee: Hydrogenics Test Systems (formerly Greenlight Power Technologies), 2004.